

Article

# Effect of Bias Voltage on Mechanical Properties of HiPIMS/RFMS Cosputtered Zr–Si–N Films

Yung-I Chen <sup>1,2</sup>, Yu-Zhe Zheng <sup>1</sup>, Li-Chun Chang <sup>3,4,\*</sup> and Yu-Heng Liu <sup>1</sup><sup>1</sup> Institute of Materials Engineering, National Taiwan Ocean University, Keelung 20224, Taiwan<sup>2</sup> Center of Excellence for Ocean Engineering, National Taiwan Ocean University, Keelung 20224, Taiwan<sup>3</sup> Department of Materials Engineering, Ming Chi University of Technology, New Taipei 24301, Taiwan<sup>4</sup> Center for Plasma and Thin Film Technologies, Ming Chi University of Technology, New Taipei 24301, Taiwan

\* Correspondence: lchang@mail.mcut.edu.tw; Tel.: +886-2-2908-9899

Received: 27 July 2019; Accepted: 20 August 2019; Published: 21 August 2019



**Abstract:** Zr–Si–N films with atomic ratios of N/(Zr + Si) of 0.54–0.82 were fabricated through high-power impulse magnetron sputtering (HiPIMS)–radio-frequency magnetron sputtering (RFMS) cosputtering by applying an average HiPIMS power of 300 W on the Zr target, various RF power levels on the Si target, and negative bias voltage levels of 0–150 V connected to the substrate holder. Applying a negative bias voltage on substrates enhanced the ion bombardment effect, which affected the chemical compositions, mechanical properties, and residual stress of the Zr–Si–N films. The results indicated that Zr–Si–N films with Si content ranging from 1.4 to 6.3 atom % exhibited a high hardness level of 33.2–34.6 GPa accompanied with a compressive stress of 4.3–6.4 GPa, an  $H/E^*$  level of 0.080–0.107, an  $H^3/E^{*2}$  level of 0.21–0.39 GPa, and an elastic recovery of 62–72%.

**Keywords:** bias voltage; elastic recovery; HiPIMS;  $H/E^*$ ;  $H^3/E^{*2}$ ; mechanical properties; residual stress; RFMS

## 1. Introduction

Nanocomposite Zr–Si–N films have attracted considerable research interest because of their mechanical properties and oxidation resistance; these films with 2–6 atom % Si exhibit a hardness level of 30–36 GPa [1–4], whereas the films with a high Si content (15–30 atom %) display remarkable oxidation resistance at 600 °C accompanied with a low hardness level of 12–16 GPa [5,6]. An nc-M<sub>n</sub>N/a-Si<sub>3</sub>N<sub>4</sub> model has been developed to estimate the hardness improvement of low-Si-content nanocomposite M–Si–N films (M: transition metal) [7–11]. Nanocrystalline M–N grains surrounded by an amorphous Si<sub>3</sub>N<sub>4</sub> matrix improve the film hardness attributed to strengthening mechanisms including solid-solution strengthening, nanocomposite formation hardening, and residual stress effect [11]. However, in contrast to Ti–Si–N films, the hardness improvement of Zr–Si–N films by adding Si to form nanocomposite films is limited [1–5]. High-power impulse magnetron sputtering (HiPIMS) with a dense plasma comprising a high degree of ionization of the sputtered materials [12–14] was used to fabricate films with a dense structure accompanied with a high hardness and high residual compressive stress [15,16]. Moreover, hybrid processes such as direct-current magnetron sputtering (HiPIMS-DCMS) [17] and radio-frequency magnetron sputtering (HiPIMS-RFMS) [18] were used to increase the deposition rate, which was a limitation of the conventional HiPIMS process [13,14]. In a previous study [19], the crystalline Zr–Si–N films of 2–6 atom % Si prepared using a HiPIMS-RFMS process showed low surface roughness (0.8–1.4 nm) and high nanoindentation hardness (33.1–34.3 GPa), Young's modulus (346–373 GPa), and compressive residual stress (4.4–5.0 GPa). Tang et al. [20] fabricated Zr–Si–N films through a hybrid system comprising a superimposed HiPIMS-medium frequency and

RF sputtering at a 200 °C substrate temperature and −100 V bias voltage; their results exhibited that the films containing 4.7 atom % Si had the highest hardness (33.4 GPa). Moreover, in our previous study [19], the hardness and Young's modulus of the HiPIMS-RFMS cosputtered Zr–Si–N films exhibited linear relationships to their compressive residual stresses ranging from −0.2 to −5.0 GPa. Therefore, it is crucial to explore increasing the mechanical properties of Zr–Si–N films, and hence, its compressive residual stress was increased through application of a negative bias voltage on the substrates during deposition. In fabricating binary nitride and carbide films through the sputtering processes, applying a negative bias voltage on substrates increased the kinetic energy of the bombarding positive ions, which resulted in the increase in the adatom mobility (ion-bombardment-enhanced diffusion), resputtering, and atomic peening [21–23]. The ion bombardment peening affected the residual stress and hardness [24]. Moreover, it induced complete phase separation of the nanocomposite M–Si–N films [25] and resputtered the light Si adatoms [26]. In this study, the residual stress of Zr–Si–N films was fabricated through the HiPIMS-RFMS hybrid process, which was increased to 8.8 GPa in compression by applying a substrate bias voltage of −150 V. The effects of substrate bias voltage on the chemical compositions, phase structures, and mechanical properties of Zr–Si–N films were investigated.

## 2. Materials and Methods

The HiPIMS-RFMS cosputtering system was illustrated in detail in a previous study [19]. The Ti and Zr targets with a diameter of 76.2 mm were connected to a pulse power supply (SPIK 2000A, Shen Chang Electric, Taipei, Taiwan), whereas the Si target with a diameter of 50.8 mm was connected to a radio-frequency power generator of 13.56 MHz. The substrate-to-target distance was 12 cm. The rotating (10 rpm) substrate holder without heating was maintained at less than 70 °C during deposition. A Ti interlayer was deposited on silicon wafers at 400 W for 40 min under a working pressure of 0.4 Pa at a steady flow of 30-sccm Ar. Zr–Si–N films were cosputtered on Ti interlayers after flowing a gas mixture of Ar and N<sub>2</sub> set at 28 and 2 sccm, respectively, into the chamber, and the working pressure was maintained at 0.4 Pa. An average HiPIMS power of 300 W was applied on the Zr target, and batches A, B, and C were prepared using RF powers of 30, 40, and 50 W, respectively, on a Si target, and the substrate bias voltage was set at 0, −50, −100, and −150 V.

The chemical compositions of the films were analyzed using a field-emission electron probe microanalyzer (FE-EPMA, JXA-8500F, JEOL, Akishima, Japan). The Ti signal from interlayers was not detected, which implied that no Si signal from substrates was detected. The film thickness was evaluated through field emission scanning electron microscopy (FE-SEM, S4800, Hitachi, Tokyo, Japan). The phases of the films were analyzed using an X-ray diffractometer (XRD, X'Pert PRO MPD, PANalytical, Almelo, The Netherlands) with Cu K $\alpha$  radiation through the grazing incidence technique with an incidence angle of 1°. Moreover, the XRD patterns for determining the texture coefficients were measured following a Bragg–Brentano scan. The surface roughness values of the films were evaluated using an atomic force microscope (DI 3100, Bruker, Santa Barbara, CA, USA). The scanning area of each image was set at 5  $\mu\text{m} \times 5 \mu\text{m}$  at a scanning rate of 1.0 Hz. The hardness ( $H$ ) and elastic modulus ( $E$ ) values of films were measured using a nanoindentation tester (TI-900 Triboindenter, Hysitron, MN, USA) equipped with a Berkovich diamond probe tip. The indentation depth was 80 nm. The  $H$  and effective Young's modulus  $E^*$  ( $E^* = E/(1 - \nu^2)$ ) values were calculated based on the Oliver and Pharr method [27], where  $\nu$  is the Poisson ratio and is set at 0.31. The elastic recovery,  $We$ , was determined from the loading–unloading curves measured using nanoindentation testing [28]. The residual stress of the films was calculated using Stoney's equation [29]. The measurements on the film curvatures were calibrated using BK7 glass plates with curvatures of 0, −0.1, and +0.1  $\text{m}^{-1}$ .

### 3. Results and Discussion

#### 3.1. Chemical Compositions and Phases

Table 1 presents the chemical compositions of Zr–Si–N films fabricated using an average HiPIMS power ( $P_{Zr}$ ) of 300 W on the Zr target, various RF powers ( $P_{Si}$ ) applied on the Si target, and negative bias voltage levels of 0–150 V connected to the substrate holder. The Zr–Si–N films were denoted as  $Zr_xSi_yN_{100-x-y}$  after ignoring the O content. All the Zr–Si–N films exhibited an atomic ratio  $[N/(Zr+Si)]$  of 0.54–0.82, which was below the stoichiometric ratio of 1.0 for ZrN. The Si content of the films in batch A decreased from 3.2 to 1.4 and 0.4 atom %, whereas the N content increased from 34.9 to 36.2 and 37.3 atom % when the negative bias voltage level was increased from 0 to 50 and 100 V, respectively. The films prepared at bias voltages of –100 V and –150 V were  $Zr_{62.3}Si_{0.4}N_{37.3}$  and  $Zr_{62.2}Si_{0.4}N_{37.4}$ , respectively, which exhibited a constant and Si-less level attributed to severe ion bombardment. In our previous study on HiPIMS-RFMS-prepared Zr–Si–N films fabricated using the same gas flow (Ar: 28 sccm,  $N_2$ : 2 sccm) at ground state [19], the Si content increased from 0 to 10 atom % accompanied with an increase in N content from 29 to 40 atom %, which was attributed to the high affinity of Si and N [11,20]. Moreover, the Si content of the samples in batches B and C exhibited decreasing tendencies with an increase in substrate bias voltage, whereas the variation in N content was not correlated with the substrate bias voltage. Furthermore, the compressive residual stress increased with an increase in the substrate bias voltage for all the three batches. Therefore, applying a negative bias voltage resulted in a decrease in Si content (Figure 1), which was attributed to the ion bombardment and resputter effect [26]. All the films prepared at a substrate bias voltage above –100 V exhibited a negligible Si content of 0.3–0.4 atom %. The deposition rates slightly decreased when a substrate bias voltage was applied. The film thickness levels were controlled at 747–1080 nm through adjustment of the deposition time after considering an indentation depth of 80 nm for evaluating the films' mechanical properties.

**Table 1.** Chemical composition, surface roughness, and residual stress of the Zr–Si–N films prepared with an average high-power impulse magnetron sputtering (HiPIMS) power of 300 W on Zr target and various RF powers on Si target at various bias voltages.

Sample	Bias (–V)	Chemical Composition (at.%)				Time (min)	T <sup>1</sup> (nm)	Ra <sup>2</sup> (nm)	Stress (GPa)
		Zr	Si	N	O				
Batch A, $P_{Si} = 30$ W									
$Zr_{61.6}Si_{3.2}N_{35.2}$	0	61.0 ± 0.4	3.2 ± 0.1	34.9 ± 0.4	0.9 ± 0.2	270	932	1.4 ± 0.1	–5.0 ± 0.4
$Zr_{62.3}Si_{1.4}N_{36.3}$	50	62.2 ± 0.2	1.4 ± 0.0	36.2 ± 0.4	0.2 ± 0.1	300	1007	1.6 ± 0.0	–6.4 ± 0.6
$Zr_{62.3}Si_{0.4}N_{37.3}$	100	62.3 ± 2.1	0.4 ± 0.0	37.3 ± 2.1	0.0 ± 0.0	300	966	1.7 ± 0.1	–6.8 ± 0.3
$Zr_{62.2}Si_{0.4}N_{37.4}$	150	62.2 ± 0.6	0.4 ± 0.0	37.4 ± 0.7	0.0 ± 0.1	300	959	1.2 ± 0.3	–8.8 ± 0.3
Batch B, $P_{Si} = 40$ W									
$Zr_{56.2}Si_{5.6}N_{38.2}$	0	55.8 ± 0.2	5.6 ± 0.1	37.9 ± 0.3	0.7 ± 0.2	230	847	0.8 ± 0.1	–4.5 ± 0.6
$Zr_{60.2}Si_{3.8}N_{36.0}$	50	58.7 ± 0.9	3.7 ± 0.1	35.1 ± 0.6	2.5 ± 0.2	220	747	0.5 ± 0.0	–5.7 ± 0.5
$Zr_{58.9}Si_{0.4}N_{40.7}$	100	58.0 ± 1.0	0.4 ± 0.1	40.1 ± 1.0	1.5 ± 0.2	300	1080	0.8 ± 0.0	–6.8 ± 0.5
Batch C, $P_{Si} = 50$ W									
$Zr_{52.2}Si_{7.6}N_{40.2}$	0	52.0 ± 1.1	7.6 ± 0.2	40.1 ± 1.3	0.3 ± 0.1	210	831	3.5 ± 0.1	–2.8 ± 0.1
$Zr_{57.6}Si_{6.3}N_{36.1}$	50	56.3 ± 1.9	6.1 ± 0.3	35.3 ± 1.8	2.3 ± 0.5	210	747	0.3 ± 0.1	–4.3 ± 0.3
$Zr_{54.8}Si_{0.3}N_{44.9}$	100	54.0 ± 2.0	0.3 ± 0.0	44.3 ± 2.1	1.4 ± 0.2	265	981	0.6 ± 0.0	–7.1 ± 0.3

<sup>1</sup> T: Thickness; <sup>2</sup> Ra: Surface roughness.

Figure 2a, Figure 3a, and Figure 4a illustrate the grazing incidence XRD (GIXRD) patterns of the films in batches A, B, and C, respectively, which display a face-centered cubic (fcc) ZrN [ICDD 00-035-0753] phase. In our previous study [19], the HiPIMS-RFMS-fabricated Zr–Si–N films with Si content less than 7.6 atom % were crystalline, whereas Zr–Si–N films with Si content more than 10 atom % had a dominant X-ray amorphous phase. Figure 2b illustrates the XRD patterns of the Zr–Si–N films in batch A obtained through Bragg–Brentano scan. The fcc (111) and (200) reflections shifted toward the left side while raising the negative bias voltage level from 0 to 150 V. The shifted ZrN

(200) reflection of the  $Zr_{62.3}Si_{1.4}N_{36.3}$  films overlapped with a Ti (002) signal. The standard intensity ratio of  $I_{(111)}:I_{(200)}:I_{(220)}$  for an fcc ZrN phase is 100:74:36. Figure 5 shows the texture coefficients  $T_c$  [23] of the Zr–Si–N films calculated using (111), (200), and (220) reflection intensities. The orientation of batch A films varied from (111) for the  $Zr_{61.6}Si_{3.2}N_{35.2}$  films prepared at a ground voltage level to (200) for the  $Zr_{62.3}Si_{1.4}N_{36.3}$  films prepared at a bias voltage of  $-50$  V and then back to (111) for the  $Zr_{62.3}Si_{0.4}N_{37.3}$  and  $Zr_{62.2}Si_{0.4}N_{37.4}$  films prepared at a bias voltage of  $-100$  and  $-150$  V, respectively. Similar variations were observed for the Bragg–Brentano XRD patterns of the films in batches B and C as shown in Figures 3b and 4b. The orientations of batch B films were (111), (200), and (111) for the films prepared at a bias voltage of 0,  $-50$ , and  $-100$  V, respectively. The orientation of batch C films was (200) for the films prepared at a bias voltage of 0 and  $-50$  V, whereas the orientation was (111) for the films prepared at a bias voltage of  $-100$  V. The  $ZrSi_2$  phase [ICDD 00-032-1499] was observed besides a ZrN phase for the films in batches B and C. Because the standard Gibbs free energy levels of ZrN,  $Si_3N_4$ , and  $ZrSi_2$  at 298 K are  $-673.398$  kJ/mol of Zr or N,  $-161.836$  kJ/mol of N, and  $-157.931$  kJ/mol of Zr [30], respectively, ZrN form preferentially, and excess Zr or N bind to Si. Moreover, the standard Gibbs free energies of  $Si_3N_4$  and  $ZrSi_2$  were also interpreted as  $-215.781$  and  $-78.966$  kJ/mol of Si, respectively, which implies that  $Si_3N_4$  is more stable than  $ZrSi_2$ . However, the surveyed Zr–Si–N films in this study exhibited high Zr and low N contents, which caused the formation of major ZrN and minor  $ZrSi_2$  phases. Sandu et al. [11,31] proposed a solubility limit of 4 atom % Si for Zr–Si–N films, and the ZrN grain size and Si solubility limit decreased by applying bias voltage. In our previous study [19], the HiPIMS-RFMS-fabricated Zr–Si–N films exhibited a Si solubility of 5.6 atom %. The three Si-less films  $Zr_{62.3}Si_{0.4}N_{37.3}$ ,  $Zr_{58.9}Si_{0.4}N_{40.7}$ , and  $Zr_{54.8}Si_{0.3}N_{44.9}$  prepared with a substrate bias voltage of  $-100$  V revealed the characteristics of ZrN films deposited through strong ion bombardment, which exhibited a strong (111) texture [15]. Figure 6 displays the lattice parameters of the Zr–Si–N films calculated using (111) reflections in Bragg–Brentano XRD patterns. The lattice parameters increased with an increase in the substrate bias voltage and were larger than the standard value of 0.45776 nm for fcc ZrN, which implies that the films fabricated under a high substrate bias voltage exhibit a high residual stress during compression. Applying a substrate bias voltage resulted in a decrease in surface roughness to less than 2 nm (Table 1), possibly accompanied with structural densification [32,33].

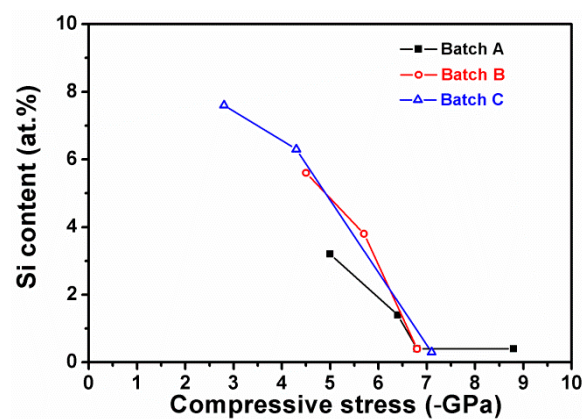


Figure 1. Relationship between Si content and residual stress of Zr–Si–N films.

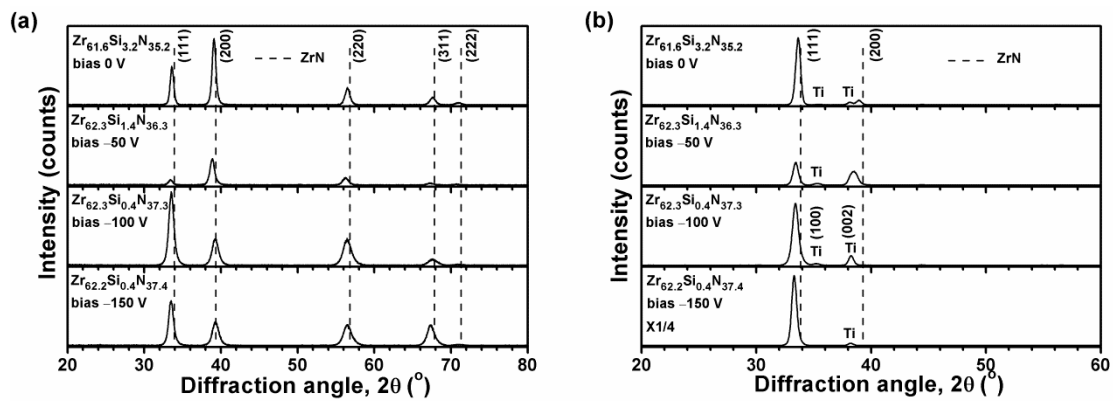


Figure 2. (a) Grazing incidence (GIXRD) and (b) Bragg–Brentano XRD patterns of the Zr–Si–N films prepared using  $P_{Zr} = 300$  W and  $P_{Si} = 30$  W on Si substrates.

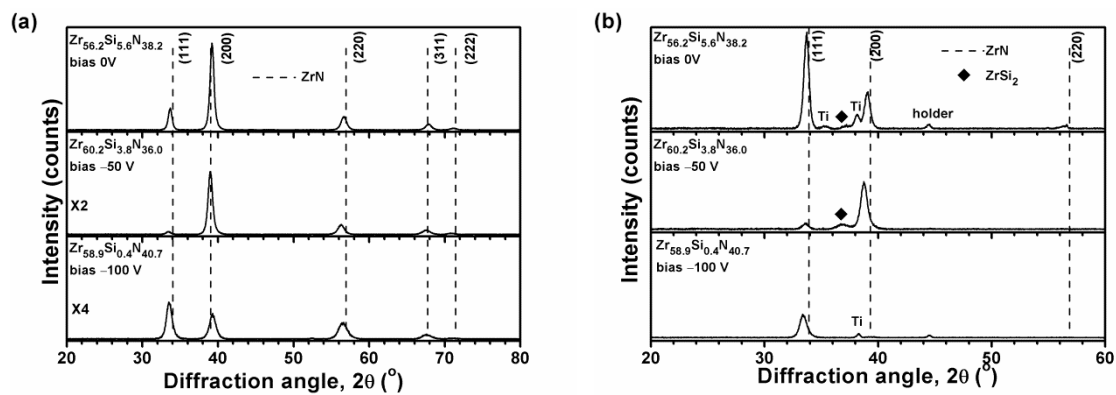


Figure 3. (a) GIXRD and (b) Bragg–Brentano XRD patterns of the Zr–Si–N films prepared using  $P_{Zr} = 300$  W and  $P_{Si} = 40$  W on Si substrates.

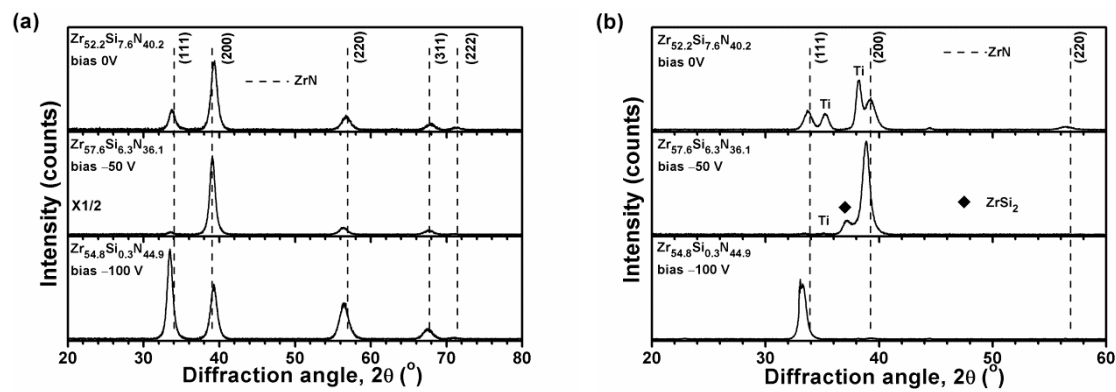


Figure 4. (a) GIXRD and (b) Bragg–Brentano XRD patterns of the Zr–Si–N films prepared using  $P_{Zr} = 300$  W and  $P_{Si} = 50$  W on Si substrates.

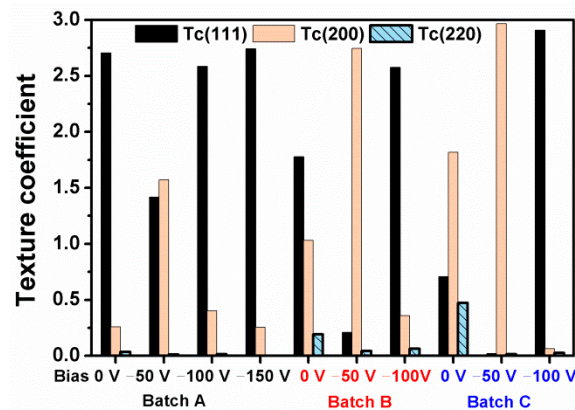


Figure 5. Texture coefficients of Zr-Si-N films.

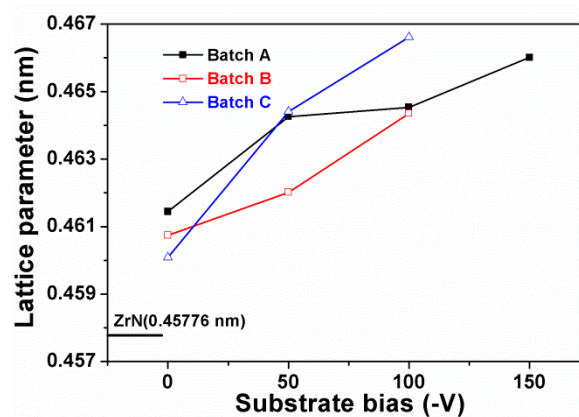


Figure 6. Lattice parameters of Zr-Si-N films fabricated under various substrate holder bias voltages.

The cross-sectional transmission electron microscopy (TEM) image of the  $Zr_{61.6}Si_{3.2}N_{35.2}$  films (batch A) prepared at a ground voltage level was displayed in a previous study [19], which exhibited a columnar structure. Figure 7a displays the cross-sectional TEM image of the  $Zr_{62.3}Si_{1.4}N_{36.3}$  films (batch A) prepared at a bias voltage of  $-50$  V, which exhibits a crystalline structure. Figure 8a displays the cross-sectional TEM image of the  $Zr_{54.8}Si_{0.3}N_{44.9}$  (batch C) prepared at a bias voltage of  $-100$  V, which exhibits a crystalline structure. Figures 7b and 8b exhibit lattice fringes of crystalline ZrN regions. All the films, namely  $Zr_{61.6}Si_{3.2}N_{35.2}$ ,  $Zr_{62.3}Si_{1.4}N_{36.3}$ , and  $Zr_{54.8}Si_{0.3}N_{44.9}$ , were crystalline, and amorphous  $Si_3N_4$  regions were not observed, which indicated that Si atoms substituted Zr atoms in the ZrN lattice as the Si contents were lower than a solubility limit [11].

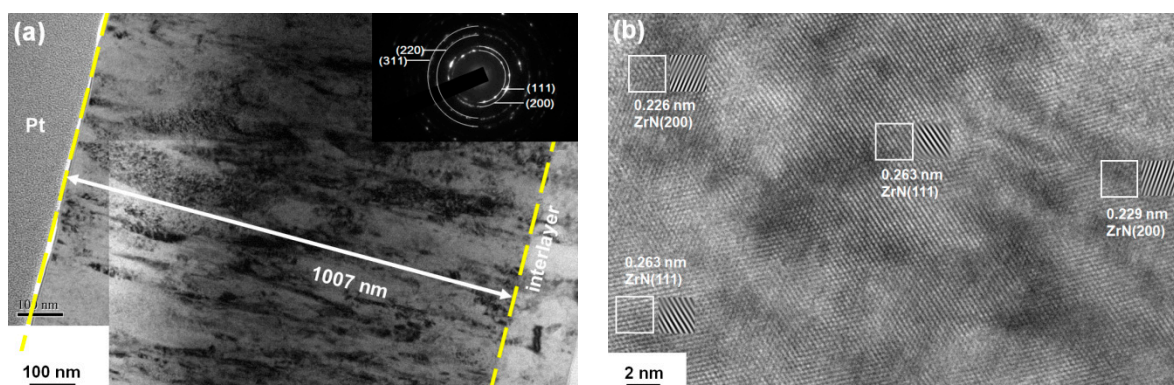
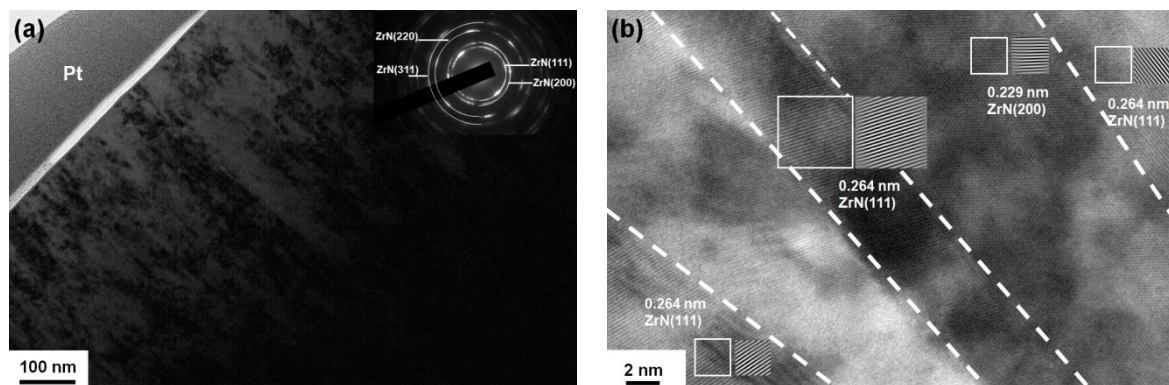


Figure 7. (a) Cross-sectional transmission electron microscopy (TEM) image and selected area electron diffraction (SAED) pattern and (b) high-resolution TEM image of the  $Zr_{62.3}Si_{1.4}N_{36.3}$  films (batch A).



**Figure 8.** (a) Cross-sectional TEM image and SAED pattern and (b) high-resolution TEM image of the  $\text{Zr}_{54.8}\text{Si}_{0.3}\text{N}_{44.9}$  films (batch C).

### 3.2. Mechanical Properties

Table 2 presents the  $H$ ,  $E^*$ ,  $H/E^*$ , and  $H^3/E^{*2}$  values of the Zr–Si–N films. Figure 9a illustrates the nanoindentation hardness values of the Zr–Si–N films with various Si contents. The films with Si content of 1.4–6.3 atom % exhibited a high hardness level (33.2–34.6 GPa). Previous studies have reported a maximum hardness of 29.8–36 GPa accompanied with an Si content of 2–6.2 atom % for Zr–Si–N films [1–3]. The  $\text{Zr}_{52.2}\text{Si}_{7.6}\text{N}_{40.2}$  film, one of the batch C films, prepared without applying a substrate bias voltage exhibited a low residual stress of  $-2.8$  GPa and showed a relatively low hardness of 27.4 GPa (Table 2). The Si content of batch C films decreased with an increase in substrate bias voltage due to the ion bombardment effect. Thus,  $\text{Zr}_{57.6}\text{Si}_{6.3}\text{N}_{36.1}$  films prepared at a bias voltage of  $-50$  V exhibited an Si content in the range of 1.4–6.3 atom % accompanied with a high hardness (33.7 GPa). Moreover, the  $\text{Zr}_{56.2}\text{Si}_{5.6}\text{N}_{38.2}$  and  $\text{Zr}_{60.2}\text{Si}_{3.8}\text{N}_{36.0}$  films (batch B) prepared at a ground voltage level and a bias voltage of  $-50$  V, respectively, exhibited an Si content of 3.8–5.6 atom % and high hardness levels of 33.2 and 34.6 GPa, respectively. Furthermore, similar results were observed for the  $\text{Zr}_{61.6}\text{Si}_{3.2}\text{N}_{35.2}$  and  $\text{Zr}_{62.3}\text{Si}_{1.4}\text{N}_{36.3}$  films (batch A), which exhibited high hardness levels of 34.3 and 34.4 GPa, respectively. By contrast, the three Si-less films,  $\text{Zr}_{62.3}\text{Si}_{0.4}\text{N}_{37.3}$  (batch A),  $\text{Zr}_{58.9}\text{Si}_{0.4}\text{N}_{40.7}$  (batch B), and  $\text{Zr}_{54.8}\text{Si}_{0.3}\text{N}_{44.9}$  (batch C), prepared at a substrate bias voltage of  $-100$  V exhibited hardness values of 29.4, 34.4, and 35.1 GPa accompanied with residual stress levels of  $-6.8$ ,  $-6.8$ , and  $-7.1$  GPa, respectively, and the films with a higher N content exhibited higher hardness. In a previous study [34], the  $\text{ZrN}_x$  films ( $x = 0.65\text{--}0.78$ ) prepared using the HiPIMS system at a  $-100$  V substrate bias voltage and a substrate temperature of  $400^\circ\text{C}$  exhibited a hardness level of 26–27 GPa accompanied with a residual stress ranging from  $-4.2$  to  $-5.2$  GPa. The  $\text{Zr}_{54.8}\text{Si}_{0.3}\text{N}_{44.9}$  films exhibited a relatively high residual stress of  $-7.1$  GPa and the highest hardness of 35.1 GPa in this study, which were comparable with the ZrN films fabricated through HiPIMS reported by Purandare et al. [15]; in their study, the samples prepared at bias voltages of  $-65$ ,  $-75$ , and  $-95$  V exhibited residual stresses of  $-5.1$ ,  $-7.7$ , and  $-10$  GPa and hardness values of 31.9, 36.6, and 40.4 GPa, respectively. Figure 9b illustrates the hardness values of Zr–Si–N films with various residual stresses, which includes some data from a previous study [19]. These data were divided into three categories according to their residual stress levels. The hardness levels of the HiPIMS-RFMS-cosputtered Zr–Si–N films exhibited a linear relationship with their residual stresses ranging from  $-0.2$  to  $-4.5$  GPa (Region I), whereas the hardness values maintained a similar level accompanied with a residual stress ranging from  $-4.5$  to  $-6.4$  GPa (Region II) and exhibited diversified values at a residual stress of more than  $-6.8$  GPa (Region III). Mae et al. [1] reported that the hardness and stress exhibited a linear trend for the ZrSiN films with stress less than  $-5$  GPa, which was a result of lattice distortion caused by the difference in the atomic sizes of Zr, Si, and N. By contrast, Qi et al. [35] reported that the hardness of ZrN coatings increased with an increase in residual stress up to 4.24 GPa in compression, and that further increasing the compressive stress to

more than 7.95 GPa resulted in a decreasing trend in hardness, which was attributed to the inverse Hall–Petch effect.

**Table 2.** Mechanical properties of the HiPIMS-RFMS-cosputtered Zr–Si–N films.

Sample	Bias (–V)	Stress (GPa)	$H^1$ (GPa)	$E^{*2}$ (GPa)	$H/E^*$	$H^3/E^{*2}$ (GPa)	$We^3$ (%)
Batch A, $P_{Si} = 30$ W							
Zr <sub>61.6</sub> Si <sub>3.2</sub> N <sub>35.2</sub>	0	$-5.0 \pm 0.4$	$34.3 \pm 1.0$	$408 \pm 12$	0.084	0.24	64
Zr <sub>62.3</sub> Si <sub>1.4</sub> N <sub>36.3</sub>	50	$-6.4 \pm 0.6$	$34.4 \pm 1.2$	$350 \pm 14$	0.098	0.33	67
Zr <sub>62.3</sub> Si <sub>0.4</sub> N <sub>37.3</sub>	100	$-6.8 \pm 0.3$	$29.4 \pm 0.6$	$346 \pm 10$	0.085	0.21	60
Zr <sub>62.2</sub> Si <sub>0.4</sub> N <sub>37.4</sub>	150	$-8.8 \pm 0.3$	$28.3 \pm 1.5$	$331 \pm 11$	0.086	0.21	60
Batch B, $P_{Si} = 40$ W							
Zr <sub>56.2</sub> Si <sub>5.6</sub> N <sub>38.2</sub>	0	$-4.5 \pm 0.6$	$33.2 \pm 1.0$	$413 \pm 13$	0.080	0.21	62
Zr <sub>60.2</sub> Si <sub>3.8</sub> N <sub>36.0</sub>	50	$-5.7 \pm 0.5$	$34.6 \pm 0.5$	$324 \pm 8$	0.107	0.39	72
Zr <sub>58.9</sub> Si <sub>0.4</sub> N <sub>40.7</sub>	100	$-6.8 \pm 0.5$	$34.4 \pm 1.0$	$413 \pm 4$	0.083	0.24	65
Batch C, $P_{Si} = 50$ W							
Zr <sub>52.2</sub> Si <sub>7.6</sub> N <sub>40.2</sub>	0	$-2.8 \pm 0.1$	$27.4 \pm 1.6$	$283 \pm 8$	0.097	0.26	63
Zr <sub>57.6</sub> Si <sub>6.3</sub> N <sub>36.1</sub>	50	$-4.3 \pm 0.3$	$33.7 \pm 0.9$	$363 \pm 6$	0.093	0.29	68
Zr <sub>54.8</sub> Si <sub>0.3</sub> N <sub>44.9</sub>	100	$-7.1 \pm 0.3$	$35.1 \pm 0.4$	$398 \pm 6$	0.088	0.27	65

<sup>1</sup>  $H$ : Hardness; <sup>2</sup>  $E^*$ : Effective Young's modulus; <sup>3</sup>  $We$ : Elastic recovery.

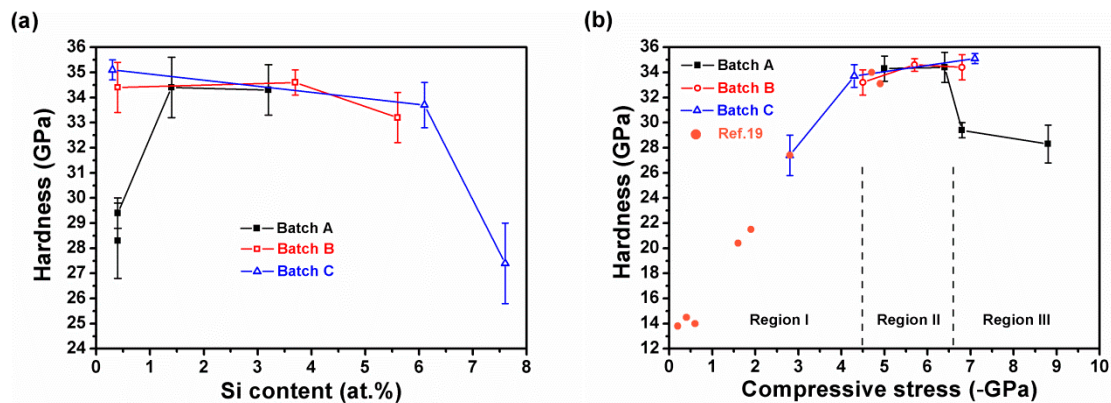


**Figure 9.** Relationships between nanoindentation hardness and (a) Si content and (b) residual stress of Zr–Si–N films.

The ratios of  $H/E$  [36–38] and  $H/E^*$  [4,39] denote elastic strain to failure, which assisted to assess the wear resistance of hard coatings with the criteria of  $H/E > 0.1$  [38] and  $H/E^* > 0.1$  [39]. Figure 10 depicts the relationship between  $H$  and  $E^*$  in which the data of the batches A, B, and C prepared at the ground state were classified as reported in Ref. 19. The data of conventional DCMS-prepared Zr–Si–N films (Ref. 5) are also shown for comparison. The HiPIMS-RFMS-cosputtered Zr–Si–N films prepared at bias voltages of  $-50$ ,  $-100$ , and  $-150$  V exhibited a high  $H/E^*$  level of  $0.083$ – $0.107$  or a high  $H/E$  level of  $0.092$ – $0.118$ . By contrast, HiPIMS-RFMS-cosputtered Zr–Si–N films prepared without applying a negative substrate bias voltage exhibited median  $H/E^*$  level of  $0.067$ – $0.097$  and  $H/E$  level of  $0.074$ – $0.107$ , whereas the DCMS-prepared Zr–Si–N films exhibited a low  $H/E^*$  level of  $0.063$ – $0.087$  and  $H/E$  level of  $0.070$ – $0.097$  accompanied with lower hardness values of  $11.7$ – $23.6$  GPa. Musil [39] proposed that hard nanocomposite films with  $H/E^* > 0.1$  and  $We \geq 60\%$  exhibited high toughness. The Zr<sub>60.2</sub>Si<sub>3.8</sub>N<sub>36.0</sub> films prepared at a bias voltage of  $-50$  V exhibited the highest  $H/E^*$  level of  $0.107$  and  $We$  level of  $72\%$  among the surveyed Zr–Si–N films in this study. In the work of Choi et al. [4], the Zr–Si (5.8 atom %)-N films exhibited the maximum hardness, Young's modulus, and  $H/E^*$  values of  $33$  GPa,  $265$  GPa, and  $0.12$ , respectively, accompanied with the lowest friction coefficient and the best wear resistance. The common characteristics of the films prepared under a substrate bias voltage of  $-50$  V exhibited

high  $H/E^*$ ,  $H^3/E^{*2}$ , and  $W_e$  values (Table 2) accompanied by (200) preferred orientation (Figure 5) as is presented in region II of Figure 9b.

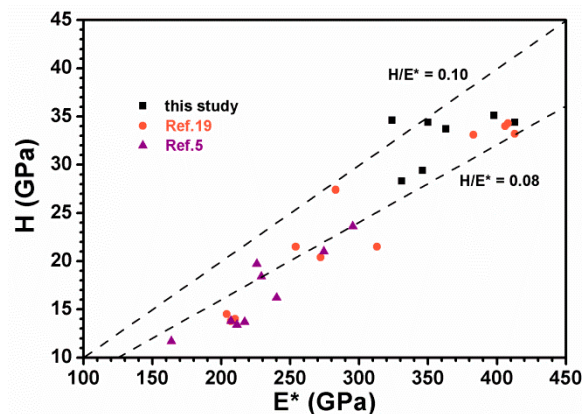


Figure 10. Relationship between hardness ( $H$ ) and effective Young's modulus ( $E^*$ ) of the Zr–Si–N coating.

The parameters of  $H^3/E^2$  [40,41] and  $H^3/E^{*2}$  [28] were widely applied to represent resistance to plastic deformation. Figure 11a presents the relationship between  $H^3/E^{*2}$  and  $H$ , which includes some data from previous studies on Zr–Si–N films [5,19]. Silva Neto et al. [42] reported that the hardness and  $H^3/E^2$  ratio exhibited an increasing trend for the DCMS- and RFMS-cosputtered Zr–Si–N films, and a maximum  $H^3/E^2$  value of 0.40 GPa was accompanied with a hardness of 20.6 GPa. In our previous study [5], DCMS-fabricated Zr–Si–N films prepared without applying a bias voltage exhibited a low  $H^3/E^{*2}$  level of <0.15 GPa ( $H^3/E^2 < 0.18$  GPa). By contrast, the HiPIMS-RFMS-cosputtered Zr–Si–N films prepared at a bias voltage of  $-50$ ,  $-100$ , and  $-150$  V exhibited high  $H^3/E^{*2}$  levels ranging from 0.21 to 0.39 GPa ( $H^3/E^2$ : 0.25–0.48 GPa), whereas the HiPIMS-RFMS-cosputtered Zr–Si–N films prepared at ground state exhibited medium  $H^3/E^{*2}$  levels ranging from 0.06 to 0.26 GPa ( $H^3/E^2$ : 0.08–0.31 GPa). A high  $H^3/E^{*2}$  level of 0.60 GPa was reported for Zr–Si–N films [43]. Figure 11b displays the relationship between  $H^3/E^{*2}$  and elastic recovery ( $W_e$ ). The  $W_e$  value increased with an increase in the  $H^3/E^{*2}$  value.

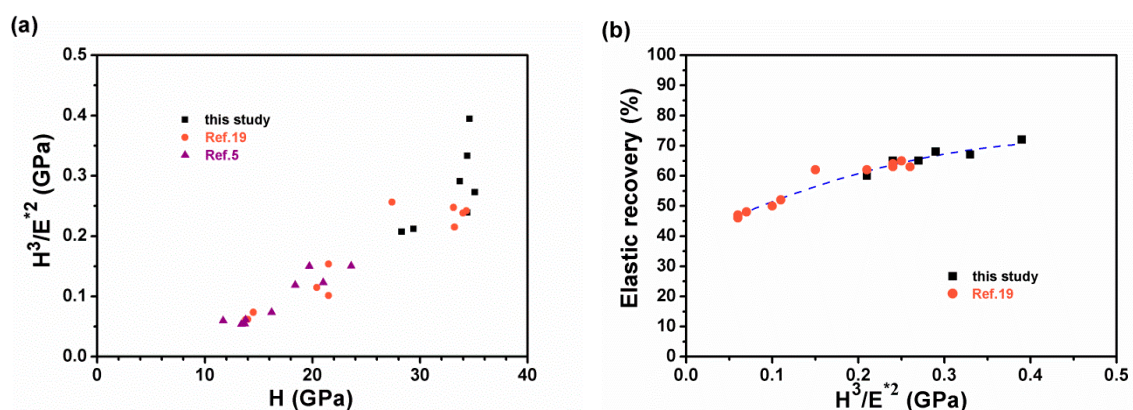


Figure 11. (a)  $H^3/E^{*2}$  ( $E^*$ : effective Young's modulus) as a function of hardness ( $H$ ) and (b) elastic recovery ( $W_e$ ) as a function of  $H^3/E^{*2}$  for Zr–Si–N films. (●: reference 19; ▲: reference 5).

#### 4. Conclusions

The effects of ion bombardment during sputtering deposition were enhanced by applying a negative bias voltage, which resulted in an increase in residual stress and a decrease in Si content for Zr–Si–N films relative to that prepared at ground state. Applying a moderate substrate bias voltage makes the Zr–Si–N films a dense structure with high mechanical properties. The hardness exhibited a linear relationship with residual stress ranging from  $-0.2$  to  $-4.5$  GPa and maintained an almost constant level with residual stress ranging from  $-4.5$  to  $-6.4$  GPa, whereas at residual stress above

–6.8 GPa, the hardness varied inconsistently. The films prepared under a substrate bias voltage of –50 V exhibited high  $H$ ,  $H/E^*$ ,  $H^3/E^{*2}$ , and  $W_e$  values accompanied with (200) preferred orientation. By contrast, the films prepared at a substrate bias voltage of more than –100 V exhibited an Si-less content, a strong (111) texture, and a high residual stress ranging from –6.8 to –8.8 GPa. Further research should focus on applying the HiPIMS-RFMS cosputtered Zr–Si–N films on the diffusion barrier utility for Cu metallization.

**Author Contributions:** Conceptualization, Y.-I.C. and L.-C.C.; Data curation, Y.-H.L.; Investigation, Y.-Z.Z.; Project administration, L.-C.C.; Resources, L.-C.C.; Validation, Y.-H.L.; Writing—original draft, Y.-I.C.

**Funding:** This research was funded by the Ministry of Science and Technology, Taiwan (107-2221-E-131-004 and 105-2221-E-019-007-MY3). The APC was funded by Ming Chi University of Technology.

**Acknowledgments:** The authors thank Mei-Chen Chiang at Ming Chi University of Technology for the technical support of TEM observations.

**Conflicts of Interest:** The authors declare no conflict of interest.

## References

- Mae, T.; Nose, M.; Zhou, M.; Nagae, T.; Shimamura, K. The effects of Si addition on the structure and mechanical properties of ZrN thin films deposited by an r.f. reactive sputtering method. *Surf. Coat. Technol.* **2001**, *142–144*, 954–958. [[CrossRef](#)]
- Martin, P.J.; Bendavid, A.; Cairney, J.M.; Hoffman, M. Nanocomposite Ti–Si–N, Zr–Si–N, Ti–Al–Si–N, Ti–Al–V–Si–N thin film coatings deposited by vacuum arc deposition. *Surf. Coat. Technol.* **2005**, *200*, 2228–2235. [[CrossRef](#)]
- Dong, Y.; Zhao, W.; Li, Y.; Li, G. Influence of silicon on the microstructure and mechanical properties of Zr–Si–N composite films. *Appl. Surf. Sci.* **2006**, *252*, 5057–5062. [[CrossRef](#)]
- Choi, H.; Jang, J.; Zhang, T.; Kim, J.H.; Park, I.W.; Kim, K.H. Effect of Si addition on the microstructure, mechanical properties and tribological properties of Zr–Si–N nanocomposite coatings deposited by a hybrid coating system. *Surf. Coat. Technol.* **2014**, *259*, 707–713. [[CrossRef](#)]
- Chen, Y.I.; Chang, S.C.; Chang, L.C. Oxidation resistance and mechanical properties of Zr–Si–N coatings with cyclic gradient concentration. *Surf. Coat. Technol.* **2017**, *320*, 168–173. [[CrossRef](#)]
- Chang, L.C.; Zheng, Y.Z.; Chen, Y.I.; Chang, S.C.; Liu, B.L. Bonding characteristics and chemical inertness of Zr–Si–N coatings with a high Si content in glass molding. *Coatings* **2018**, *8*, 181. [[CrossRef](#)]
- Veprek, S.; Niederhofer, A.; Moto, K.; Bolom, T.; Männling, H.-D.; Nesladek, P.; Dollinger, G.; Bergmaier, A. Composition, nanostructure and origin of the ultrahardness in nc-TiN/a-Si<sub>3</sub>N<sub>4</sub>/a- and nc-TiSi<sub>2</sub> nanocomposites with  $H_V = 80$  to  $\geq 105$  GPa. *Surf. Coat. Technol.* **2000**, *133–134*, 152–159. [[CrossRef](#)]
- Diserens, M.; Patscheider, J.; Lévy, F. Mechanical properties and oxidation resistance of nanocomposite TiN–SiN<sub>x</sub> physical-vapor-deposited thin films. *Surf. Coat. Technol.* **1999**, *120–121*, 158–165. [[CrossRef](#)]
- Benkahoul, M.; Sandu, C.S.; Tabet, N.; Parlinska-Wojtan, M.; Karimi, A.; Lévy, F. Effect of Si incorporation on the properties of niobium nitride films deposited by DC reactive magnetron sputtering. *Surf. Coat. Technol.* **2004**, *188–189*, 435–439. [[CrossRef](#)]
- Sandu, C.S.; Benkahoul, M.; Sanjinés, R.; Lévy, F. Model for the evolution of Nb–Si–N thin films as a function of Si content relating the nanostructure to electrical and mechanical properties. *Surf. Coat. Technol.* **2006**, *201*, 2897–2903. [[CrossRef](#)]
- Sandu, C.S.; Sanjinés, R.; Benkahoul, M.; Medjani, F.; Lévy, F. Formation of composite ternary nitride thin films by magnetron sputtering co-deposition. *Surf. Coat. Technol.* **2006**, *201*, 4083–4089. [[CrossRef](#)]
- Kouznetsov, V.; Macák, K.; Schneider, J.M.; Helmersson, U.; Petrov, I. A novel pulsed magnetron sputter technique utilizing very high target power densities. *Surf. Coat. Technol.* **1990**, *122*, 290–293. [[CrossRef](#)]
- Helmersson, U.; Lättemann, M.; Bohlmark, J.; Ehiasarian, A.P.; Gudmundsson, J.T. Ionized physical vapor deposition (IPVD): A review of technology and applications. *Thin Solid Films* **2006**, *513*, 1–24. [[CrossRef](#)]
- Gudmundsson, J.T.; Brenning, N.; Lundin, D.; Helmersson, U. High power impulse magnetron sputtering discharge. *J. Vac. Sci. Technol. A* **2012**, *30*, 030801. [[CrossRef](#)]
- Purandare, Y.P.; Ehiasarian, A.P.; Hovsepian, P.E. Structure and properties of ZrN coatings deposited by high power impulse magnetron sputtering technology. *J. Vac. Sci. Technol. A* **2011**, *29*, 011004. [[CrossRef](#)]

16. Ehiasarian, A.P.; Münz, W.-D.; Hultman, L.; Helmersson, U.; Petrov, I. High power pulsed magnetron sputtered CrN<sub>x</sub> films. *Surf. Coat. Technol.* **2003**, *163–164*, 267–272. [[CrossRef](#)]
17. Greczynski, G.; Lu, J.; Jensen, J.; Bolz, S.; Kölker, W.; Schiffers, C.; Lemmer, O.; Greene, J.E.; Hultman, L. A review of metal-ion-flux-controlled growth of metastable TiAlN by HIPIMS/DCMS co-sputtering. *Surf. Coat. Technol.* **2014**, *257*, 15–25. [[CrossRef](#)]
18. Chang, L.C.; Chang, C.Y.; You, Y.W. Ta–Zr–N thin films fabricated through HIPIMS/RFMS co-sputtering. *Coatings* **2017**, *7*, 189. [[CrossRef](#)]
19. Chang, L.C.; Zheng, Y.Z.; Chen, Y.I. Mechanical properties of Zr–Si–N films fabricated through HiPIMS/RFMS co-sputtering. *Coatings* **2018**, *8*, 263. [[CrossRef](#)]
20. Tang, Q.L.; Wu, Y.C.; Lou, B.S.; Chen, Z.Y.; Lee, J.W. Mechanical property evaluation of ZrSiN films deposited by a hybrid superimposed high power impulse- medium frequency sputtering and RF sputtering system. *Surf. Coat. Technol.* **2019**. [[CrossRef](#)]
21. Sundgren, J.-E.; Johansson, B.-O.; Hentzell, H.T.G.; Karlsson, S.-E. Mechanisms of reactive sputtering of titanium nitride and titanium carbide III: Influence of substrate bias on composition and structure. *Thin Solid Films* **1983**, *105*, 385–393. [[CrossRef](#)]
22. Petrov, I.; Hultman, L.; Helmersson, U.; Sundgren, J.-E.; Greene, J.E. Microstructure modification of TiN by ion bombardment during reactive sputter deposition. *Thin Solid Films* **1989**, *169*, 299–314. [[CrossRef](#)]
23. Lee, H.C.; Lee, J.Y.; Ahn, H.J. Effect of the substrate bias voltage on the crystallographic orientation of reactively sputtered AlN thin films. *Thin Solid Films* **1994**, *251*, 136–140. [[CrossRef](#)]
24. Wang, H.; Zhang, S.; Li, Y.; Sun, D. Bias effect on microstructure and mechanical properties of magnetron sputtered nanocrystalline titanium carbide thin films. *Thin Solid Films* **2008**, *516*, 5419–5423. [[CrossRef](#)]
25. Vaz, F.; Rebouta, L.; Goudeau, P.; Girardeau, T.; Pacaud, J.; Rivière, J.P.; Traverse, A. Structural transitions in hard Si-based TiN coatings: The effect of bias voltage and temperature. *Surf. Coat. Technol.* **2001**, *146–147*, 274–279. [[CrossRef](#)]
26. Yang, Z.T.; Yang, B.; Guo, L.P.; Fu, D.J. Effect of bias voltage on the structure and hardness of Ti–Si–N composite coatings synthesized by cathodic arc assisted middle-frequency magnetron sputtering. *J. Alloy. Compd.* **2009**, *473*, 437–441. [[CrossRef](#)]
27. Oliver, W.C.; Pharr, G.M. An improved technique for determining hardness and elastic modulus using load and displacement sensing indentation experiments. *J. Mater. Res.* **1992**, *7*, 1564–1583. [[CrossRef](#)]
28. Musil, J.; Kunc, F.; Zeman, H.; Poláková, H. Relationships between hardness, Young’s modulus and elastic recovery in hard nanocomposite coatings. *Surf. Coat. Technol.* **2002**, *154*, 304–313. [[CrossRef](#)]
29. Janssen, G.C.A.M.; Abdalla, M.M.; van Keulen, F.; Pujada, B.R.; van Venrooy, B. Celebrating the 100th anniversary of the Stoney equation for film stress: Developments from polycrystalline steel strips to single crystal silicon wafers. *Thin Solid Films* **2009**, *517*, 1858–1867. [[CrossRef](#)]
30. Barin, I. *Thermochemical Data of Pure Substances*, 3rd ed.; VCH: New York, NY, USA, 1995.
31. Sandu, C.S.; Cusnir, N.; Oezer, D.; Sanjinés, R.; Patscheider, J. Influence of bias voltage on the microstructure and physical properties of magnetron sputtered Zr–Si–N nanocomposite thin films. *Surf. Coat. Technol.* **2009**, *204*, 969–972. [[CrossRef](#)]
32. Lee, J.W.; Tien, S.K.; Kuo, Y.C. The effects of pulse frequency and substrate bias to the mechanical properties of CrN coatings deposited by pulsed DC magnetron sputtering. *Thin Solid Films* **2006**, *494*, 161–167. [[CrossRef](#)]
33. Wang, Z.; Zhang, D.; Ke, P.; Liu, X.; Wang, A. Influence of substrate negative bias on structure and properties of TiN coatings prepared by hybrid HIPIMS method. *J. Mater. Sci. Technol.* **2015**, *31*, 37–42. [[CrossRef](#)]
34. Chang, L.C.; Chang, C.Y.; Chen, Y.I.; Kao, H.L. Mechanical properties and oxidation behavior of ZrN<sub>x</sub> thin films fabricated through high-power impulse magnetron sputtering deposition. *J. Vac. Sci. Technol. A* **2016**, *34*, 02D107. [[CrossRef](#)]
35. Qi, Z.B.; Sun, P.; Zhu, F.P.; Wang, Z.C.; Peng, D.L.; Wu, C.H. The inverse Hall–Petch effect in nanocrystalline ZrN coatings. *Surf. Coat. Technol.* **2011**, *205*, 3692–3697. [[CrossRef](#)]
36. Leyland, A.; Matthews, A. On the significance of the *H/E* ratio in wear control: A nanocomposite coating approach to optimised tribological behavior. *Wear* **2000**, *246*, 1–11. [[CrossRef](#)]
37. Liu, K.Y.; Lee, J.W.; Wu, F.B. Fabrication and tribological behavior of sputtering TaN coatings. *Surf. Coat. Technol.* **2014**, *259*, 123–128. [[CrossRef](#)]

38. Pogrebnjak, A.D.; Beresnev, V.M.; Bondar, O.V.; Postolnyi, B.O.; Zaleski, K.; Coy, E.; Jurga, S.; Lisovenko, M.O.; Konarski, P.; Rebuta, L.; et al. Superhard CrN/MoN coatings with multilayer architecture. *Mater. Des.* **2018**, *153*, 47–59. [[CrossRef](#)]
39. Musil, J. Hard nanocomposite coatings: Thermal stability, oxidation resistance and toughness. *Surf. Coat. Technol.* **2012**, *207*, 50–65. [[CrossRef](#)]
40. Tsui, T.Y.; Pharr, G.M.; Oliver, W.C.; Bhatia, C.S.; White, R.L.; Anders, S.; Anders, A.; Brown, I.G. Nanoindentation and nanoscratching of hard carbon coatings for magnetic disks. *Mater. Res. Soc. Symp. Proc.* **1995**, *383*, 447–452. [[CrossRef](#)]
41. Liu, C.Y.; Diyatmika, W.; Lou, B.S.; Lu, Y.C.; Duh, J.G.; Lee, J.W. Influences of target poisoning on the mechanical properties of TiCrBN thin films grown by a superimposed high power impulse and medium-frequency magnetron sputtering. *Surf. Coat. Technol.* **2017**, *332*, 86–95. [[CrossRef](#)]
42. Silva Neto, P.C.; Freitas, F.G.R.; Fernandez, D.A.R.; Carvalho, R.G.; Felix, L.C.; Terto, A.R.; Hubler, R.; Mendes, F.M.T.; Silva Junior, A.H.; Tentardini, E.K. Investigation of microstructure and properties of magnetron sputtered Zr-Si-N thin films with different Si content. *Surf. Coat. Technol.* **2018**, *353*, 355–363. [[CrossRef](#)]
43. Musil, J.; Daniel, R.; Zeman, P.; Takai, O. Structure and properties of magnetron sputtered Zr-Si-N films with a high ( $\geq 25$  at.%) Si content. *Thin Solid Films* **2005**, *478*, 238–247. [[CrossRef](#)]



© 2019 by the authors. Licensee MDPI, Basel, Switzerland. This article is an open access article distributed under the terms and conditions of the Creative Commons Attribution (CC BY) license (<http://creativecommons.org/licenses/by/4.0/>).